Velocity-tunable beam of continuously decelerated polar molecules for cold ion-molecule reaction studies

James Greenberg, O. A. Krohn, Jason A. Bossert, et al.

View Online   Export Citation   CrossMark

ARTICLES YOU MAY BE INTERESTED IN

Development and characterization of high-repetition-rate sources for supersonic beams of fluorine radicals
Review of Scientific Instruments **92**, 103203 (2021); https://doi.org/10.1063/5.0065498

A digital feedback system for advanced ion manipulation techniques in Penning traps
Review of Scientific Instruments **92**, 103201 (2021); https://doi.org/10.1063/5.0064369

A simple and effective attachment to prevent dome diffraction reaching 2D or 1D detectors in x-ray diffractometers
Review of Scientific Instruments **92**, 103102 (2021); https://doi.org/10.1063/5.0052057

Velocity-tunable beam of continuously decelerated polar molecules for cold ion-molecule reaction studies

James Greenberg,[1,2] (iD) O. A. Krohn,[1,2] (iD) Jason A. Bossert,[1,2] (iD) Yomay Shyur,[1,2,3] (iD) David Macaluso,[1,2,4]
N. J. Fitch,[1,2,5] (iD) and H. J. Lewandowski[1,2,a)] (iD)

AFFILIATIONS

[1] Department of Physics, University of Colorado, Boulder, Colorado 80309, USA
[2] JILA, National Institute of Standards and Technology and University of Colorado, Boulder, Colorado 80309, USA
[3] Harvard John A. Paulson School of Engineering and Applied Sciences, Cambridge, Massachusetts 02138, USA
[4] Department of Physics and Astronomy, University of Montana, Missoula, Montana 59812, USA
[5] Centre for Cold Matter, Blackett Laboratory, Imperial College London, Prince Consort Road, London SW7 2AZ, United Kingdom

[a)] Author to whom correspondence should be addressed: lewandoh@colorado.edu

ABSTRACT

Producing high densities of molecules is a fundamental challenge for low-temperature, ion-molecule reaction studies. Traveling-wave Stark decelerators promise to deliver high density beams of cold, polar molecules but require non-trivial control of high-voltage potentials. We have overcome this experimental challenge and demonstrate continuous deceleration of ND_3 from 385 to 10 m/s, while driving the decelerator electrodes with a 10 kV amplitude sinewave. In addition, we test an alternative slowing scheme, which increases the time delay between decelerated packets of ND_3 and non-decelerated molecules, allowing for better energy resolution of subsequent reaction studies. We characterize this source of neutral, polar molecules suitable for energy-resolved reaction studies with trapped ions at cold translational temperatures. We also propose a combined apparatus consisting of the traveling-wave decelerator and a linear ion trap with a time-of-flight mass spectrometer and discuss to what extent it may achieve cold, energy-resolved, ion-neutral reactions.

Published under an exclusive license by AIP Publishing. https://doi.org/10.1063/5.0057859

I. INTRODUCTION

Studies of gas-phase, low-temperature ion-molecule reactions can elucidate chemical processes in the interstellar medium and provide insight into the fundamental mechanisms of bond breaking and formation. One major focus of research in these fields is understanding the rich diversity of organic molecules observed in space, where ion-molecule reactions play a critical role.[1–8] Laboratory experiments improve models of interstellar gas clouds, circumstellar shells, and planetary atmospheres by characterizing the products of ion-molecule reactions under extreme conditions of low-temperature and low pressure environments. Such efforts work toward an understanding of the formation of an incredible range of chemical species in extra-terrestrial conditions.

Cold reaction experiments can explore the impact of quantum mechanical effects, including tunneling and scattering resonances.[9–13] Often, reaction outcomes can be controlled by the choice

of the initial quantum state.[14–17] In addition, fine control of the collision energy allows for benchmarking of quantum chemical calculations and thermochemistry, further refining theoretical methods as a result of increasing experimental precision.

Advances in our theoretical descriptions of reaction studies are sometimes driven by the results of low-temperature studies.[9,18,19] Low-temperature ion-molecule reactions are usually barrierless and thus have reaction kinetics that are often determined purely by capture rates. The associated reaction kinetics can exhibit counter-intuitive dependencies on temperature. Some reactions proceed faster at low temperatures, while others freeze out entirely due to potential energy barriers.[20,21] Investigations into reaction dynamics probe the underlying potential energy surfaces. These experimental observations help reveal novel reaction mechanisms and benchmark the accuracy of quantum chemical calculations of such surfaces.[22,23]

Experimental realizations of low-temperature, ion-molecule reactions typically face the fundamental challenge that reactant

densities are low for both ion and neutral species. The ion densities are low because they are limited by space-charge effects. In addition, producing cold neutral molecules at high densities continues to be a challenge, especially for radical species, which are challenging to produce *in situ*. The combined low density samples lead to small reaction rates, thus requiring long interaction times to produce measurable product quantities. Experiments involving ion traps (to increase the time for interactions) and specialized Stark decelerators (for dense neutral molecular beams) are well-suited to overcome this challenge.

Stark decelerators can provide a source of tunable-velocity neutral molecules (including radicals) for ion-molecule experiments.[24–26] The source for the decelerator is typically a supersonic expansion of molecules, which has a very narrow velocity distribution. Based on the phase-space acceptance of the Stark decelerator, only a portion of the original distribution is selected, resulting in packets of molecules being guided or slowed. However, a conventional pulsed-pin decelerator[24] suffers from low densities at low velocities due to complex coupling between longitudinal and transverse confinement.[27] This may be addressed with the use of a traveling-wave Stark decelerator (TWSD) as it provides slowed packets with true continuous 3D confinement, as well as a larger phase-space acceptance volume.[28–38] These TWSDs produce significant densities of molecules even at the lowest collision velocities for ion-molecule reaction experiments.

One particularly useful system for studying ion-molecule reactions is a linear Paul ion trap radially coupled to a time-of-flight mass spectrometer (LIT-TOFMS), where reactions can be studied over long timescales with excellent sensitivity to product ions.[39–42] These experiments create cold molecular ions by co-trapping them with laser-cooled atomic ions, which serve as an ultracold temperature bath for collisional cooling. A previously successful method employs Stark velocity filters of effusive molecule sources at room temperature.[43,44] Unfortunately, the experiments are plagued by vanishing densities at the lowest collision velocities. The low density is the direct result of the effusive sources that feed into the velocity filters, which have Boltzmann distributions close to room temperature. Therefore, there are not many low-velocity molecules present in the beam. The addition of cold neutral molecule sources with tunable velocities allows for improved low-temperature ion-neutral reaction studies.

Thus, we propose to combine a TWSD with an LIT-TOFMS, via a molecular beam shutter and guiding hexapole (see Fig. 1). The TWSD is able to slow a variety of polar species to low beam velocities, while the ion trap provides a cold ion target. In addition, a degree of quantum-state control could arise from both the decelerator and guiding hexapole, which can be selected for individual

quantum states of the neutral molecule.[45] Finally, the ion trap allows for long interaction times (up to several minutes) with detection efficiency near unity of all trapped ions, including product ions.

Here, we characterize the TWSD side of the proposed, combined apparatus. First, we describe our TWSD experiment. This includes a description of the decelerator, its operation at ±10 kV, and the detection scheme for the slowed beam of ND_3. We then present the results of continuous slowing from 385 to 10 m/s. We also show measurements of an alternative slowing scheme designed to increase the separation between decelerated and non-decelerated molecules. Following this is a discussion of the implications of the presented results on future low-temperature ion-molecule studies in the proposed, combined apparatus. Finally, we make concluding remarks, including the near future of the experiment.

II. EXPERIMENT

The central component of the experiment is the TWSD. The TWSD apparatus remains mostly unchanged from previous descriptions.[36,46,47] Ammonia (ND_3), diluted to 2% in krypton, is admitted into an ultra-high vacuum (UHV) source chamber by a piezoelectric actuated molecular beam valve.[48] We use a valve backing pressure of 20 PSIG and a valve opening time of 100 μs. This produces a pulsed, supersonic beam, which is then collimated by a 2 mm diameter skimmer ~20 cm downstream of the valve. The skimmer allows for differential pumping between the source and decelerator chambers (also at UHV, 10^{-9} Torr). The first of 624 rings in the decelerator is 3 mm beyond the back edge of the skimmer in the decelerator chamber. The rings are made of 1.02 mm diameter tantalum wire with a 4 mm diameter clear aperture through which the molecules propagate and a center-to-center spacing of 2.03 mm. Every eighth ring of the decelerator is electrically connected by stainless steel support rods. Each set of eight rings is referred to as a "stage." The decelerator has 78 stages.

Deceleration of a portion of the molecular beam is achieved by forces produced from a potential energy well that moves along with the molecular beam with a decreasing speed. Molecules with a velocity close to the speed of the potential well experience a force opposite the direction of their motion and thus slow down. The wells are created via spatially and temporally varying sinusoidal electrical potentials applied to the support rods.[36] Each of the eight support rods is connected to an independent home-built, high-voltage amplifier. While the amplifiers have also previously been described in detail,[37,46] two major changes to the amplifiers and their operation enable their performance with an amplitude of 10 kV. The first alteration was the exchange of the main optical isolator for one with a higher voltage rating (TT Electronics/Optek Technology OPI150). This optical isolator transfers the control signal from the low-voltage computer control board to the high-voltage side of the amplifier. Second, we have changed the deceleration waveform to protect the amplifiers from fast voltage transients. Previously, the amplifiers were abruptly shut off before molecular detection. Now, they continue to oscillate for three cycles while the amplitude decays exponentially to zero. In addition, we now operate the amplifiers at a 2 Hz repetition rate due to limitations of the current sourcing backing capacitors. These changes have allowed us to apply a linearly chirped sinewave with 10 kV amplitude to the rods and subsequently produce a co-moving potential well to continuously

FIG. 1. Simplified rendering of the proposed, combined apparatus. Following the TWSD is an in-vacuum molecular beam shutter. The decelerated beam admitted through the shutter is guided by a hexapole and focused into the ion trap.

slow ND_3. The starting and ending frequencies of the chirp are varied between 30 kHz and DC to match desired initial and final velocities. Alternatively, a sinewave can be held at a particular frequency, which creates a co-moving potential well at a fixed velocity. Guiding molecular packets at a fixed velocity is referred to as bunching.

We detect ND_3 at the exit of the decelerator with a single stage, time-of-flight mass spectrometer (TOFMS). Parallel steel plates with a 5 mm hole centered on the molecular beam axis are used as a repeller and extractor for the TOFMS. The repeller plate is 7 mm from the final decelerator ring and held at a constant 2 kV while the extractor plate is grounded. Approximately 30 cm downstream is a multichannel plate (MCP) ion detector (Jordan TOF) at −3.2 kV. ND_3 is ionized in the region between the repeller and extractor plates by a 2 + 1 resonance enhanced, multiphoton ionization (REMPI) scheme at 317 nm. We produce 317 nm light with a pulsed dye amplifier (PDA, Liop-TEC). A continuous-wave, narrow linewidth (~1 MHz) Ti:sapphire seed laser (M Squared SolsTiS) at 784 nm is amplified with LDS 789 dye, diluted in pure ethanol. The dye is pumped by pulsed 532 nm light from a seeded Nd:YAG (Quanta-Ray Lab 160 Pro). This creates pulsed 784 nm light with the linewidth Fourier-limited by the duration of the pump laser pulse (10 ns). Finally, the pulsed 784 nm is combined with excess 532 nm in a Beta barium borate (BBO) crystal to produce 0.6 mJ/pulse of 317 nm light, which is focused (~40 μm spot size) onto the molecular beam. The resulting ND_3^+ ions are accelerated toward the MCP and arrive within a narrow time window as recorded by an oscilloscope. The oscilloscope trace is background subtracted and integrated in time to determine the relative density of ND_3 in the beam.

The ND_3 density as a function of arrival time at the end of the decelerator is taken by varying the time delay between triggers for the pulsed molecular valve and ionization laser q-switch. For each time delay, 16 oscilloscope traces are recorded, and the relative density is averaged. The pulsed valve and ionization lasers are triggered at a 10 Hz repetition rate by a master digital delay generator (DDG) running off its internal clock. A separate DDG running at 2 Hz triggers the amplifiers/deceleration sequence and oscilloscope. A divide-by-five counter circuit synchronizes the two clocks with negligible delay.

III. RESULTS

A. Continuous deceleration of ND_3 from 385 to 10 m/s

Packets of decelerated ND_3 molecules were detected after being slowed from an initial velocity of 385 m/s to multiple final velocities. Different final velocities, ranging from 300 to 10 m/s, were chosen to demonstrate the tunability of the beam produced by the TWSD. We expect the ND_3 signal to be the sum of the decelerated packet with a background of non-decelerated molecules, which exit the decelerator at the same time. To account for the contribution from the non-decelerated ND_3 molecules, we first measured the signal while the decelerator electrodes were grounded. We refer to this measurement as the free-flight data. We then scale the free-flight data to the background value of the decelerated data to be able to evaluate the portion of the signal from non-decelerated molecules. We must scale the free-flight data for two reasons. First, the MCP voltage needs to have a different setting for these different datasets to avoid saturating the detector. Second, the overall number of non-decelerated molecules that reach the end of the decelerator during a deceleration sequence will be larger (than in free flight), as they are transversely guided. Figure 2 shows a summary of the deceleration data, as well as the free-flight data, scaled to match the decelerated data baseline. Combined, these data show the contribution from free-flight molecules is negligible for final velocities ≤100 m/s. The decelerated packets of ND_3 also show four or five distinct peaks at each final velocity. These correspond to multiple potential wells being filled in the decelerator. We verified that the final velocity of the molecules in each well is the same by comparing the detection time of each peak with the ending time of the deceleration sequence. Using the fixed distance between ring electrodes, and the distance between the final ring of the decelerator and the TOFMS extraction region, we found precise agreement between calculated and measured peak arrival times of each of the peaks in the molecular packets.

As the final velocity of the molecular packet decreases, the measured width of each packet increases (see Fig. 2). This increase is caused by the spread of velocities of the molecules within each decelerated well. The velocity spread was modeled in a previous
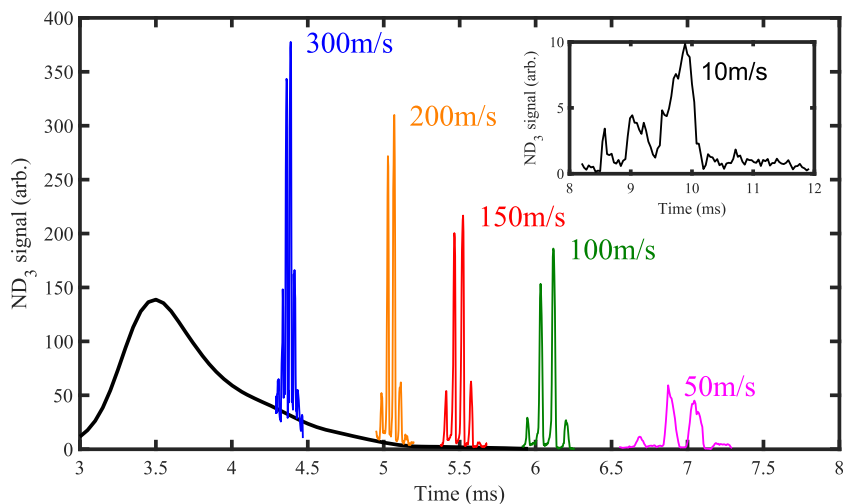

FIG. 2. Deceleration data for multiple final velocities ranging from 300 to 10 m/s. Time is the delay between the molecular beam valve trigger and the detection laser pulse. The solid black trace is the free-flight data, as discussed in the main text, scaled to match the baseline of the deceleration data. The free-flight background is essentially zero by 6 ms. The inset plot shows the 10 m/s data. The discrete peaks at each final velocity correspond to multiple, filled potential wells all with the same longitudinal velocity.

TABLE I. Maximum longitudinal spread in velocities of ND_3 wells at the end of the decelerator, as calculated by the LPSA model. The full-width half max velocity spread, which is more relevant to collision studies, will be less than this and depends on how the phase-space distribution overlaps with the phase-space acceptance of the decelerator. The velocity spread for $v_f = 385$ m/s is from bunching. Velocity spreads are also converted into kinetic energy uncertainties to facilitate discussion of the energy resolution obtained for collision studies.

v_f (m/s)	Δv (m/s)	ΔE (μeV)
385	22	49
300	17	31
200	13	18
150	12	14
100	11	12
50	10	10
10	10	10

FIG. 3. Measured and modeled number of molecules, normalized, as a function of final velocity. The black circles represent the data scaled by the reduction in the number of molecules from the exit of the last decelerator ring to the position of the laser due to transverse spread. The red squares represent the total area of the LPSA model, normalized to the area of the LPSA model at 300 m/s. Note the decreasing velocity axis and the lines connecting the points are just to guide the eye.

study using a longitudinal phase-space acceptance (LPSA) model.[36] The model showed quantitative agreement with full molecular trajectory simulations,[36,49,50] so we apply it here to estimate a maximum velocity spread for each molecular packet. The details of the model are included in the Appendix A. The key feature is that the TWSD creates a potential energy well in the radial dimension that is independent of the deceleration applied. Thus, changes in the longitudinal potential primarily impact the dynamics of deceleration. The phase-space acceptance along the axis of the decelerator can be directly calculated as a function of the average force of deceleration. This gives the largest possible spread of phase-stable, and thus decelerated, molecules. The results from the LPSA model are tabulated in Table I. The calculations show that the velocity spread of the molecules leaving the decelerator is typically small, ~10 m/s. The transverse spread in velocities has been investigated previously[36] and is also on the order of ~10 m/s.

We can compare the total number of molecules detected at each final velocity to estimate the overall decelerator efficiency and compare it to the results from the LPSA model. We calculate the total number of decelerated molecules by subtracting the scaled free-flight background from the deceleration data, integrating in time over all of the peaks, normalizing by the final velocity to account for the extended time for slower packets of molecules, and including the impact of detecting the molecules downstream from the exit of the decelerator (see Appendix B for details). The resulting integrated number of molecules detected as a function of final velocity is shown in Fig. 3 by black circles.

Finally, we predict how much integrated molecule signal we expect to see based on the LPSA model. The total area of the LPSA should scale the same as the total number of molecules detected, assuming that the transverse confinement is entirely decoupled from the longitudinal confinement, and the decelerator phase-space acceptance is filled uniformly. The results of the model calculations, also shown in Fig. 3, show good agreement with the experimental results. Ultimately, we see the decelerator retains nearly half of the molecules all the way down to 10 m/s, which is a very favorable result for collision studies with trapped ions. The experimental and modeled results are sufficient for planning future reactions with the decelerated beam as discussed below.
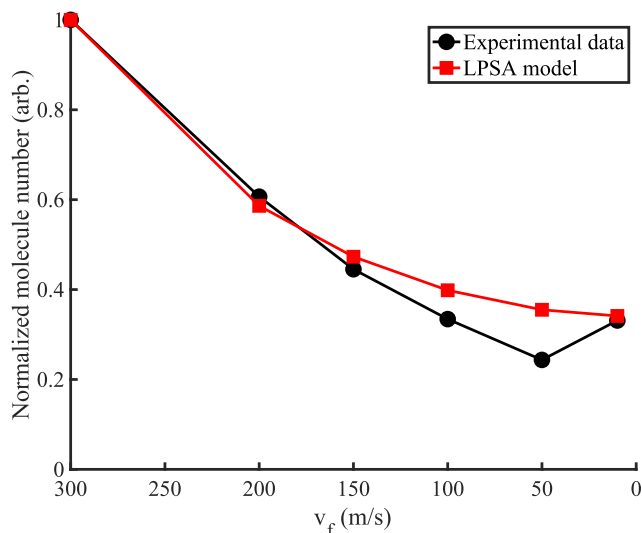
B. Alternative slowing scheme

One requirement to make Stark-decelerated beams useful for energy-resolved reaction experiments is for the non-decelerated molecules to be separated from the decelerated packet. If the two distributions of molecules can be sufficiently separated in time, then a molecular beam shutter can be placed in the beam path to allow only decelerated molecules through. For low-velocity packets, this time is large enough while running the decelerator in the typical manner. However, for higher final velocity packets, an alternate slowing scheme must be employed.

The typical slowing scheme uses the entire length of the decelerator for slowing, which produces the largest number of slow molecules. Here, we test an alternative slowing scheme that decelerates the molecules more aggressively than necessary, using only a fraction of the decelerator's length for slowing, and the rest of the decelerator for bunching at the final velocity. The end effect is an increase in the time delay between decelerated and non-decelerated molecules (including carrier gas) exiting the decelerator. This alternative slowing scheme has been previously demonstrated with ND_3 in a pin decelerator.[51] Here, we report the time delay and increased energetic purity of the molecular packets exiting the TWSD as a result of using the alternate scheme.

To test the alternative slowing approach, we vary the number of decelerator stages (1 stage = 8 rings) used for slowing vs bunching to study ND_3 decelerated to a final velocity of 250 m/s. A summary of these results are shown in Fig. 4. A free-flight background was also measured and scaled to the decelerated data baseline as discussed above. We are able to achieve a time delay from the typical scheme of around 800 μs, which corresponds to a delay between the peak of the molecular beam and the decelerated molecules of 1.7 ms. This is
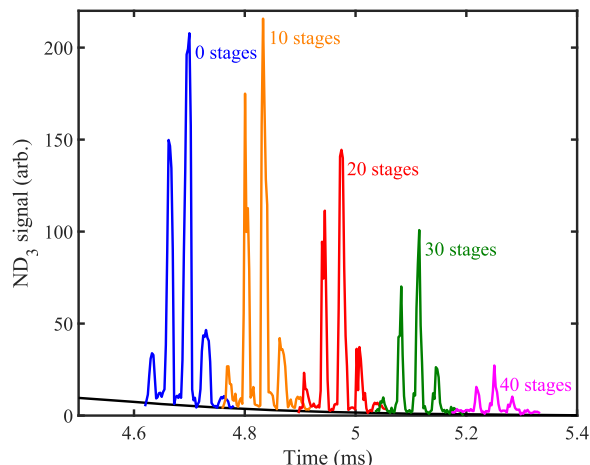
FIG. 4. Deceleration data for a final velocity of 250 m/s using the alternative slowing scheme. The time axis represents the delay between the molecular beam valve and detection laser triggers. The free-flight data are scaled to match the baseline of the deceleration data. As the number of bunching stages increases, more aggressive deceleration is applied to the molecular beam, which reaches the final velocity in a shorter distance. This leads to a time delay in the arrival of the slowed packets of ND_3.
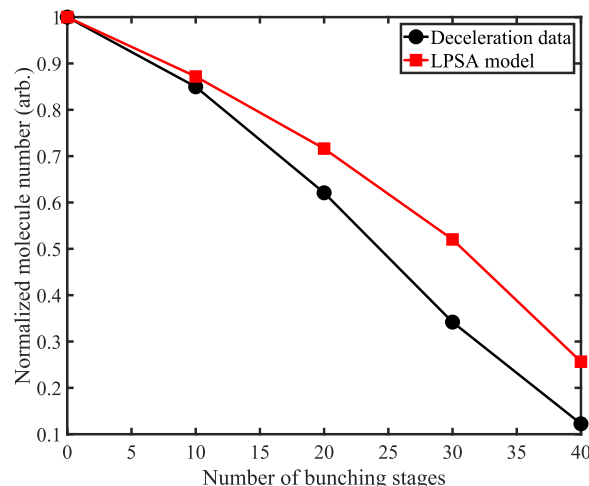

FIG. 5. Measured and modeled number of molecules, normalized, as a function of the number of bunching stages. The black circles are the integrated ND_3 signal, normalized to the integrated signal using zero bunching stages. The red squares represent the total area of the LPSA model, normalized to the area of the LPSA model using zero bunching stages. All points represent molecules decelerated to 250 m/s. The data at zero bunching stages correspond to the typical deceleration scheme.

more than enough delay as typical shutter opening times are around 500 μs (Uniblitz, LS series). We also verified that the final velocity of the molecules was in fact 250 m/s for all molecular packets shown, as discussed in Sec. III A.

There is, however, a clear trade-off between the amount of time delay gained by increasing the number of bunching stages (i.e., more aggressive slowing) and the integrated ND_3 signal. To quantify this effect, we subtract the free-flight background and integrate the decelerated peaks. The integrated ND_3 signal as a function of bunching stages is plotted in Fig. 5 and normalized to the zero bunching stage data point, which corresponds to our typical deceleration scheme. We also calculate the LPSA area to predict the decrease in the integrated ND_3 signal. The smallest LPSA calculated used 40 bunching stages, which corresponds to a deceleration aggressive enough to change the propagation direction of the molecules (molecular packet travels back toward the valve), provided the entire length of the decelerator is used. The well depth associated with such aggressive deceleration is only 0.05 K.

In addition to increasing the time between the peak of the molecular beam and the decelerated signal to allow for a shutter to be implemented, we want to optimize the decelerated beam for velocity purity. For a metric to quantify the velocity purity, we choose the percentage of decelerated molecules that are included in the total integrated signal. To calculate this, we integrate the signal above the free-flight background and divide it by the total integrated signal. Doing this for the alternative slowing data results in the data points shown in Fig. 6. This analysis reveals that 20 bunching stages is the optimal choice for velocity purity of a beam at 250 m/s.

There is a limitation to the application of bunching after the deliberately aggressive slowing scheme. The amount of time delay added per bunching stage is proportional to the final slowing velocity. This means that less time delay can be achieved for higher final velocities. For example, with v_f = 300 m/s, only 400 μs can be

added before the slowed packet signal vanishes, which is predicted by a vanishing potential well. This example, verified experimentally, uses only eight stages of the decelerator for slowing and thus 70 stages for bunching. This is unfortunate from a velocity purity standpoint because there is more background at earlier times. However, two possible solutions utilize the TWSD ability to slow ND_3 more aggressively than needed to bring the molecules to rest. Instead
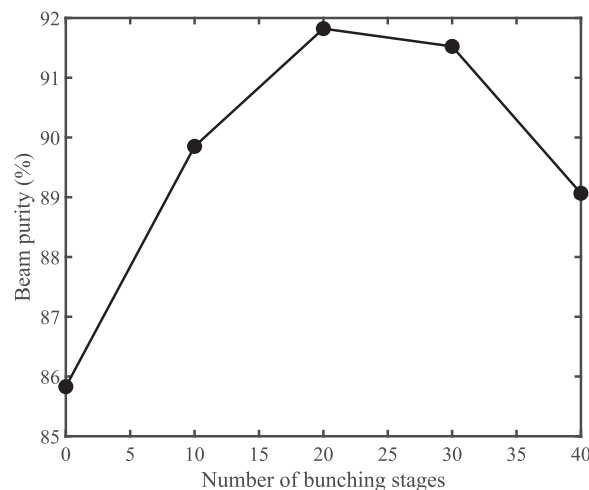

FIG. 6. Purity of the molecular beam defined as the percentage of decelerated molecules out of all molecules detected within the integrated time window containing the molecular packet. The number of decelerated molecules decreases at a different rate as compared to the non-decelerated molecular beams with an increasing number of bunching stages. For a final velocity of 250 m/s, the maximum purity corresponds to 20 bunching stages.

of bunching after such a deceleration, one can allow the molecular packet to turn around and be guided back toward the start of the decelerator. Upon arrival at the upstream edge of the decelerator, the packet can be turned around again and accelerated back to the desired final velocity by the time it reaches the end of the decelerator. This scheme (a so called "bounce") has been demonstrated in a TWSD with CH_3F molecules.[35] Another solution involves decelerating the molecular packet to rest before the end of the decelerator. There, it can be trapped for the desired delay time and then re-accelerated to the final velocity of choice.[32,33]

IV. DISCUSSION

In this section, we discuss the direct implications of our results on future cold ion-molecule reaction studies that are presented in Fig. 1, specifically the ability to study the effect of collision energy for cold, quantum-state resolved reactions, including the resulting reaction rates. We anticipate reaching low translational temperatures, defined by

$$T_{coll} = \frac{E_{coll}}{k_B} = \frac{\mu v_{rel}^2}{2k_B},$$
(1)

where μ is the reduced mass of the reactants, v_{rel} is the relative velocity between reactants, and k_B is Boltzmann's constant. If the trapped, laser-cooled (or sympathetically cooled) ions are assumed to be stationary, v_{rel} is equivalent to the TWSD final velocity. To estimate the temperature scale from this assumption, consider the reaction $ND_3^+ + ND_3 \rightarrow ND_4^+ + ND_2$. Here, $\mu = m_{ND_3}/2$, and v_{rel} can range from 385 to 10 m/s. Evaluating Eq. (1) with these parameters yields a temperature range from 90 to < 1 K. This would not be the first experiment to achieve ion-molecule reactions in this temperature regime (see references in Ref. 9) but would allow for nearly continuous tunability over this range. In addition, the selection of cold neutral species produced by a TWSD includes many polar molecules and, in particular, some radicals. Ion traps also have major flexibility in the species of molecular ions that can be loaded and sympathetically cooled. Since the reactions between radicals and ions are notoriously understudied, especially at cold temperatures, realization of the proposed, combined experiment would offer an exciting extension to the current field.

Being particularly interested in reactions between radicals and ions, we have tabulated the lowest reaction temperatures attainable using our TWSD for a few species of interest in Table II. These values assume that the lowest velocity attainable by the TWSD is limited by a calculated deceleration well depth of 0.05 K and $\mu = m_{radical}/2$.

TABLE II. Minimum final velocities and minimum reaction temperatures for other radicals that can be decelerated using our TWSD apparatus. These assume a minimum well depth of 0.05 K, as calculated by the LPSA model using molecular constants from Refs. 26, 46, 52, and 53.

Radical	v_f (m/s)	T_{coll} (K)
NO $\lvert X^2\Pi_{1/2}, J = 1/2, M\Omega = -1/4\rangle$	270	65
OH $\lvert X^2\Pi_{3/2}, J = 3/2, M\Omega = -9/4\rangle$	0	<1
CH $\lvert X^2\Pi_{1/2}, J = 1/2, M\Omega = -1/4\rangle$	0	<1
NH $\lvert a^1\Delta, J = 2, M = 2\rangle$	0	<1
SH $\lvert X^2\Pi_{3/2}, J = 3/2, M\Omega = -9/4\rangle$	285	80

The ultimate lower limit to the reaction temperature may also be affected by two other sources of translational motion. The first is the transverse velocity spread of the TWSD beam, subsequently guided by the hexapole. Previous studies of the TWSD indicate this contribution to be on the order of 10 m/s.[36,46] This could increase the collision energy as much as a factor of two. The second is the motion of the ions. So far, we have treated them as a stationary target. Reactions between trapped ions and Stark velocity filtered molecules have shown that the radial micromotion of ions could be the dominant source of kinetic energy below 30 K.[43] However, the effect can be mitigated completely by using an ion string, which experiences no micromotion, as the ions lie along the electric field node. In fact, ion micromotion can be leveraged as a way to tune the collision energy at low velocities (demonstrated in Refs. 16 and 43). Thus, we view the motion of the ions as a feature of the combined apparatus, rather than just a detriment.

Reaction studies that utilize a molecular beam from the TWSD will also benefit from excellent energy resolution. In Table I, the uncertainty in beam energy is at most 50 μeV. This allows for precision tests of reaction thermochemistry, which can be used to benchmark quantum chemical calculations. Practically, one could scan the collision energy over a range where reaction products change from exothermic to endothermic. For example, the charge exchange between laser-cooled Ca^+ and NO would be an excellent candidate experiment as whether or not the reaction is exothermic is within the limits of theoretical uncertainty.[14]

One additional benefit is that the Stark deceleration process's efficiency depends on the particular quantum states.[45] State selectivity can be realized by taking advantage of the different Stark shifts for different quantum states and can be further enhanced through the guiding hexapole. Assuming significant density losses are not incurred by such filtration, the dynamics of reactions between specific quantum states can be investigated.

Overall, the success of future reaction dynamics experiments hinges on the TWSD beam density. If the density of slowed molecules from the TWSD is too low, reactions will take place on a timescale that is too long to maintain the stability of the experiment. This point is demonstrated by the example reaction from before, $ND_3^+ + ND_3 \rightarrow ND_4^+ + ND_2$, which occurs at a rate given by

$$\frac{d[ND_3^+]}{dt} = k[ND_3^+][ND_3],$$
(2)

where k is the reaction rate constant, $[ND_3^+]$ is the number of ND_3^+ in the ion trap as a function of time, and $[ND_3]$ is the density of ND_3 passing through the ion trap as a function of time. Equation (2) can be separated and integrated to obtain

$$\ln\left(\frac{[ND_3^+]}{[ND_3^+]_{t=0}}\right) = k \int_0^t [ND_3](t')\, dt'.$$
(3)

Since the decelerator delivers $[ND_3]$ packets at a set repetition rate, Eq. (3) can be simplified to

$$\ln\left(\frac{[ND_3^+]}{[ND_3^+]_{t=0}}\right) = kRI_{[ND_3]}t,$$
(4)

where R is the decelerator repetition rate, and $I_{[ND_3]}$ is given by

$$I_{[ND_3]} = \int_0^T [ND_3](t)\, dt, \qquad (5)$$

which is the density of the decelerated beam; integrated over time, it takes one pulse to pass the through the ion trap, T. If we assume an integrated density of $I_{[ND_3]} \sim 10^6$ s/cm^3, then $k \sim 10^{-9}$ cm^3/s and $R = 2$ Hz allow us to evaluate Eq. (4). The total time it will take for 90% of the reactants to deplete $([ND_3^+]/[ND_3^+]_{t=0} = 0.1)$ is $t \sim 10^3$ s, which is a reasonable timescale for trapped ion reaction experiments.

Unfortunately, we lack the experimental tools to measure the absolute density of our beam in the current experiment. We do, however, believe we can achieve $I_{[ND_3]} \sim 10^6$ s/cm^3 for a few qualitative reasons. First, densities of this magnitude have been measured out of a pulsed-pin decelerator. One group utilized calibrated laser-induced fluorescence measurements to determine the peak density of packets decelerated to several hundred m/s, which was found to be $(2 \pm 0.8) \times 10^8$ molecules/cm^3 for OH.[54] We expect the deceleration efficiency of the TWSD to show a marked improvement over pin decelerators in this regime because, as Fig. 3 demonstrates, the decelerated signal does not exhibit significant losses at low velocities. Second, the guiding hexapole will focus the decelerated beam in the transverse dimensions, which will further enhance the density of neutral molecules within the ion trap.[55] Finally, the TWSD produces many filled wells for each packet of molecules. These can be seen as the multiple discrete peaks in Figs. 2 and 4. Each peak in the packet increases the integrated density. These factors combined should allow us to achieve an average ND$_3$ density of 10^9 cm^{-3} for a duration of 1 ms. The success of the other radical sources considered (see Table II) will depend on the ability to produce comparable decelerated beam densities. Cold buffer gas beam sources may be required for certain radical species.[49]

Furthermore, the proposed combined apparatus may allow for lower beam densities than prescribed above. The LIT-TOFMS measures both the depletion of the charged reactants and growth of charged products, simultaneously.[56] Under such conditions, bimolecular reaction rates can be determined typically without the need to follow a reaction to 90% completion. Instead, we only need to wait for 10% of the ions to react, which drastically reduces the time of the full experiment for lower density beams.

V. CONCLUSIONS AND FUTURE DIRECTIONS

In summary, we have characterized a source of neutral polar molecules for use in future low-temperature ion-molecule experiments. Specifically, we achieved continuous deceleration of ND$_3$ from 385 to 10 m/s without incurring a significant loss of molecules. We have also shown that the decelerated beam can be separated from the free-flight background in time through the use of an alternative slowing scheme. This led to an enhancement in final beam velocity purity at the cost of a smaller longitudinal phase-space acceptance and thus fewer molecules. We then explored the implications of these results on future proposed ion-molecule reaction studies. Ultimately, the performance of the TWSD indicates low-temperature studies will be possible between many species of neutral polar molecules/radicals and trapped ions.

The next step toward colder ion-molecule reaction studies will be to combine the TWSD and LIT-TOFMS as shown in the proposed apparatus (see Fig. 1). This requires *in situ* characterization of the performance and transmission efficiency of both the in-vacuum shutter and hexapole guide. Measurements of the decelerated beam density would also be an interesting avenue of study. Barring the inclusion of a femtosecond laser to utilize the technique demonstrated in Ref. 35, a benchmark reaction such as $ND_3^+ + ND_3 \rightarrow ND_4^+ + ND_2$ could be used to determine integrated density as the reaction rate constants have already been studied as a function of collision velocity.[57] Following initial characterization, the laser-induced reaction $Ca^+ + NO \rightarrow NO^+ + Ca$ would be a compelling candidate for a radical-ion reaction dynamics study. These future studies will certainly push the boundaries of what is currently accessible experimentally, as well as what is understood theoretically.

AUTHOR DECLARATIONS

Conflict of Interest

The authors have no conflicts to disclose.

DATA AVAILABILITY

The data that support the findings of this study are available from the corresponding author upon reasonable request.

APPENDIX A: LONGITUDINAL PHASE-SPACE ACCEPTANCE MODEL

Results of the following longitudinal phase-space acceptance (LPSA) model are presented in the main text. To calculate the longitudinal potential of the ring decelerator, we first model it as a set of toroidal electrodes held at fixed potentials. The on-axis potential for a single torus (reproduced from Ref. 58) is given by

$$V(z) = \frac{2V_0}{\pi} \sqrt{\frac{1}{1 + z^2/a^2}} \sum_{p=0}^{\infty} (2 - \delta_{0p}) \frac{Q_{p-1/2}(\cosh(\eta_0))}{p_{p-1/2}(\cosh(\eta_0))}$$

$$\times \cos\left(p \arccos\left(\frac{z^2 - a^2}{z^2 + a^2}\right)\right), \qquad (A1)$$

where δ_{0p} is the Kronecker delta function, $a = r_0 \sinh(\eta_0)$ is the effective mean radius of equivalent ring of charge, $\eta_0 = \ln\left(\frac{R}{r_0} + \sqrt{\left(\frac{R}{r_0}\right)^2 - 1}\right)$ represents a toroidal surface with cross-sectional radius $r_0 = 5$ μm and mean radius $R = 2.5$ mm, and $V_0 = 10$ kV. $P_{p-1/2}$ and $Q_{p-1/2}$ are the associated Legendre functions of the first and second kind, respectively, where $p \leq 2$ was evaluated. $Q_{p-1/2}(\cosh(\eta_0))$ will necessarily return a complex number for all orders of p. Only the real part contributes to the on-axis potential.
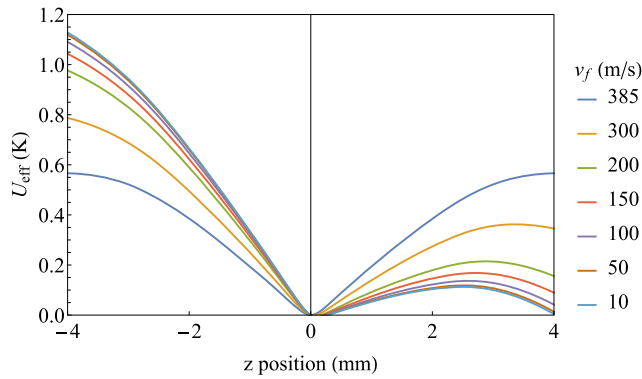
FIG. 7. Effective potential energy in Kelvin as a function of longitudinal position in the decelerated well for the different final velocities measured in the experiment. $v_f = 385$ m/s is also evaluated to show the maximum well depth experienced by the molecules during bunching, where the potential well moves at a constant speed.

Next, we sum over a set of rings with a spatially varying potential given by

$$V_{tot}(z) = \sum_{n=-N_0}^{N_0} V(z - n\,d) \cos\left(\frac{2\pi n}{8}\right), \qquad (A2)$$

where the distance between rings is $d = 2.032$ mm and $N_0 = 6$ was used. This gives quantitative agreement with the on-axis potential generated by a full, 3D model of the decelerator obtained using the COMSOL Multiphysics package.[59] The electric field is then given by $E(z) = -\frac{dV_{tot}(z)}{dz}$ and used to calculate the Stark energy. For the low-field seeking state of ND_3 $|J = 1, K = 1, MK = -1\rangle$, this is given by

$$U_{Stark}(z) = -\frac{U_{inv}}{2} + \sqrt{\left(\frac{U_{inv}}{2}\right)^2 + \left(\frac{\mu_d E(z)}{2}\right)^2}, \qquad (A3)$$

where $U_{inv} = 0.053$ cm^{-1} is umbrella mode splitting and $\mu_d = 1.48$ D is the dipole moment.[46] Equation (A3) can be used to plot the longitudinal well experienced by ND_3 molecules in the decelerator. To determine the LPSA, three more steps are needed. First, the force
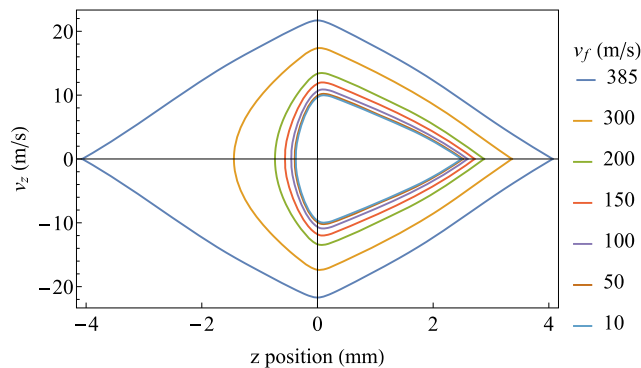
of deceleration is calculated and applied to the longitudinal well, creating an effective potential energy well given by

$$U_{eff}(z) = U_{Stark}(z) + m\,a\,z, \qquad (A4)$$

where

$$a = \frac{v_f^2 - v_i^2}{2L} \qquad (A5)$$

depends on the final velocity v_f, the initial velocity $v_i = 385$ m/s, and the length used for decelerating $L = 78 \times 8 \times d = 1.27$ m. Figure 7 shows this effective potential well for different final velocities out of the decelerator. Second, the separatrix is calculated by the classical turning points of the effective potential well. The separatrices corresponding to the final velocities in the experiment are shown in Fig. 8. Finally, the LPSA is then calculated by the area enclosed by the longitudinal separatrix. The LPSAs for the alternative slowing scheme shown in Fig. 5 were calculated using a fixed value of $v_f = 250$ m/s and by varying the length of the decelerator $L = (78 - B) \times 8 \times d$, where B is the number of bunching stages.

APPENDIX B: CALCULATION OF THE TOTAL NUMBER OF MOLECULES DETECTED

To compare the experimental measurements to the results from the LPSA, we must model the way we detect our molecules. The detection laser beam is located 7 mm downstream from the last decelerator ring. Thus, as the molecules travel to the detection region, they spread out in the transverse dimensions due to the residual transverse velocity spread. Since the lower velocity molecules have more time to spread out transversely, fewer of them
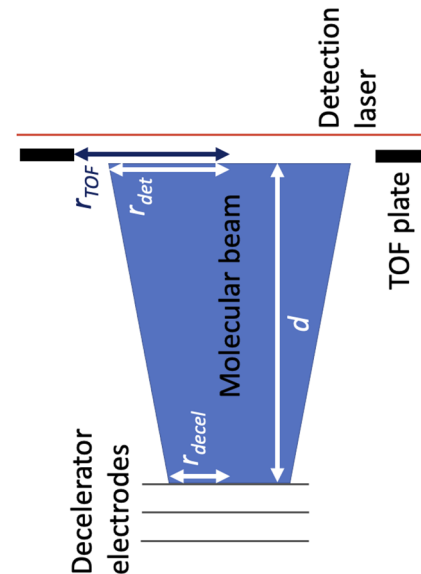

FIG. 9. Cross-sectional view of the end of the decelerator and detection region with the propagation of the molecular beam shown in blue. The molecular beam propagates from the exit of the decelerator to the detection laser, spreading from an initial radius r_{decel} to radius r_{det} at the detection region. Depending on the amount of transverse spread, there may be clipping due to the radius of the TOF aperture, r_{TOF}. Figure not to scale.

FIG. 8. Longitudinal separatrices resulting from the effective potentials in Fig. 7.

cross the detection laser beam. To accurately compare the relative number of molecules out of the decelerator for different final velocities, we must include the impact of this spreading of the molecular packet.

To estimate the consequences of this spreading, we make a few assumptions. The first assumption is that the molecular packets have a transverse velocity ($v_\perp$) equal to 10 m/s. Using this, the transverse radius of the packet at the detection region, r_{det}, is described by the following equation (see Fig. 9):

$$r_{\text{det}} = r_{\text{decel}} + \frac{v_\perp}{v_\parallel} \cdot d, \tag{B1}$$

where d is the 7 mm distance from the exit of the decelerator to the ionization laser, $v_\parallel$ is the mean longitudinal speed of the packet, and r_{decel} is the radius of the packet at the end of the decelerator, which is taken to be 2 mm. We also assume that our 317 nm laser has a beam waist much smaller than the diameter of the molecular packet and it has a sufficiently long Rayleigh length such that it can ionize molecules along the diameter of the molecular packet. In this case, the ratio of molecules at the output the decelerator (N_{decel}) to those in the detection region (N_{det}) scales with the inverse of the ratio of the radius of the molecular packets,

$$\frac{N_{\text{decel}}}{N_{\text{det}}} = \frac{r_{\text{det}}}{r_{\text{decel}}} = \frac{r_{\text{decel}} + \frac{v_\perp}{v_\parallel} \cdot d}{r_{\text{decel}}}. \tag{B2}$$

In addition, the aperture in the TOF plates is 2.5 mm and will clip molecular packets that have expanded beyond this opening. In this case, the number of molecules detected will be reduced as follows:

$$\frac{N_{\text{decel}}}{N_{\text{det}}} = \frac{r_{\text{det}}}{r_{\text{decel}}} \cdot \frac{r_{\text{det}}}{r_{\text{TOF}}} = \frac{\left(r_{\text{decel}} + \frac{v_\perp}{v_\parallel} \cdot d\right)^2}{r_{\text{decel}} \cdot r_{\text{TOF}}}, \tag{B3}$$

where r_{TOF} is the radius of the aperture.

We find this to affect molecular packets with a longitudinal velocity that meets the following criteria:

$$v_\parallel \leq \frac{d \cdot v_\perp}{r_{\text{TOF}} - r_{\text{decel}}}. \tag{B4}$$

Thus, the clipping of the molecular packet happens for final velocities at or below 130 m/s. In Fig. 3, we reported the number of molecules (black circles) scaled by the factors in Eq. (B2), if the final decelerated velocity is greater than 130 m/s, or in Eq. (B3) for the case where it is less than 130 m/s.

REFERENCES

[1] C. P. Endres, S. Schlemmer, P. Schilke, J. Stutzki, and H. S. P. Müller, J. Mol. Spectrosc. **327**, 95 (2016).

[2] P. Ehrenfreund, M. Spaans, and N. G. Holm, Philos. Trans. R. Soc., A **369**, 538 (2011).

[3] E. Herbst and E. F. van Dishoeck, Annu. Rev. Astron. Astrophys. **47**, 427 (2009).

[4] W. Klemperer, Annu. Rev. Phys. Chem. **62**, 173 (2011).

[5] V. Vuitton, R. V. Yelle, S. J. Klippenstein, S. M. Hörst, and P. Lavvas, Icarus **324**, 120 (2019).

[6] S. S. R. Offner, B. A. L. Gaches, and J. R. Holdship, Astrophys. J. **883**, 121 (2019).

[7] S. A. Fuselier, K. Altwegg, H. Balsiger, J. J. Berthelier, A. Bieler, C. Briois, T. W. Broiles, J. L. Burch, U. Calmonte, G. Cessateur, M. Combi, J. De Keyser, B. Fiethe, M. Galand, S. Gasc, T. I. Gombosi, H. Gunell, K. C. Hansen, M. Hässig, A. Jäckel,
A. Korth, L. Le Roy, U. Mall, K. E. Mandt, S. M. Petrinec, S. Raghuram, H. Rème, M. Rinaldi, M. Rubin, T. Sémon, K. J. Trattner, C.-Y. Tzou, E. Vigren, J. H. Waite, and P. Wurz, Astron. Astrophys. **583**, A2 (2015).

[8] G. J. Molina-Cuberos, H. Lichtenegger, K. Schwingenschuh, J. J. López-Moreno, and R. Rodrigo, J. Geophys. Res.: Planets **107**, 9-1, https://doi.org/10.1029/2000je001480 (2002).

[9] B. R. Heazlewood and T. P. Softley, Nat. Rev. Chem. **5**, 125 (2021).

[10] P. C. Schmid, J. Greenberg, T. L. Nguyen, J. H. Thorpe, K. J. Catani, O. A. Krohn, M. I. Miller, J. F. Stanton, and H. J. Lewandowski, Phys. Chem. Chem. Phys. **22**, 20303 (2020).

[11] R. J. Shannon, M. A. Blitz, A. Goddard, and D. E. Heard, Nat. Chem. **5**, 745 (2013).

[12] R. T. Skodje, D. Skouteris, D. E. Manolopoulos, S.-H. Lee, F. Dong, and K. Liu, Phys. Rev. Lett. **85**, 1206 (2000).

[13] W. Dong, C. Xiao, T. Wang, D. Dai, X. Yang, and D. H. Zhang, Science **327**, 1501 (2010).

[14] J. Greenberg, P. C. Schmid, M. Miller, J. F. Stanton, and H. J. Lewandowski, Phys. Rev. A **98**, 032702 (2018).

[15] H. Li, S. Jyothi, M. Li, J. Kłos, A. Petrov, K. R. Brown, and S. Kotochigova, Phys. Chem. Chem. Phys. **22**, 10870 (2020).

[16] P. Puri, M. Mills, I. Simbotin, J. A. Montgomery, R. Côté, C. Schneider, A. G. Suits, and E. R. Hudson, Nat. Chem. **11**, 615 (2019).

[17] S. Ospelkaus, K.-K. Ni, D. Wang, M. H. G. de Miranda, B. Neyenhuis, G. Quéméner, P. S. Julienne, J. L. Bohn, D. S. Jin, and J. Ye, Science **327**, 853 (2010).

[18] G. K. Chen, C. Xie, T. Yang, A. Li, A. G. Suits, E. R. Hudson, W. C. Campbell, and H. Guo, Phys. Chem. Chem. Phys. **21**, 14005 (2019).

[19] J. Toscano, H. J. Lewandowski, and B. R. Heazlewood, Phys. Chem. Chem. Phys. **22**, 9180 (2020).

[20] V. Zhelyazkova, F. B. V. Martins, J. A. Agner, H. Schmutz, and F. Merkt, Phys. Rev. Lett. **125**, 263401 (2020).

[21] R. Plasil, T. Mehner, P. Dohnal, T. Kotrik, J. Glosik, and D. Gerlich, Astrophys. J. **737**, 60 (2011).

[22] Z. Yang, Y. Mao, and M. Chen, J. Phys. Chem. A **125**, 235 (2021).

[23] S. N. Vogels, T. Karman, J. Kłos, M. Besemer, J. Onvlee, A. van der Avoird, G. C. Groenenboom, and S. Y. T. van de Meerakker, Nat. Chem. **10**, 435 (2018).

[24] H. L. Bethlem, G. Berden, and G. Meijer, Phys. Rev. Lett. **83**, 1558 (1999).

[25] S. Y. T. van de Meerakker, H. L. Bethlem, N. Vanhaecke, and G. Meijer, Chem. Rev. **112**, 4828 (2012).

[26] H. L. Bethlem, F. M. H. Crompvoets, R. T. Jongma, S. Y. T. van de Meerakker, and G. Meijer, Phys. Rev. A **65**, 053416 (2002).

[27] B. C. Sawyer, B. K. Stuhl, B. L. Lev, J. Ye, and E. R. Hudson, Eur. Phys. J. D **48**, 197 (2008).

[28] S. A. Meek, H. Conrad, and G. Meijer, Science **324**, 1699 (2009).

[29] A. Osterwalder, S. A. Meek, G. Hammer, H. Haak, and G. Meijer, Phys. Rev. A **81**, 051401 (2010).

[30] S. A. Meek, M. F. Parsons, G. Heyne, V. Platschkowski, H. Haak, G. Meijer, and A. Osterwalder, Rev. Sci. Instrum. **82**, 093108 (2011).

[31] N. E. Bulleid, R. J. Hendricks, E. A. Hinds, S. A. Meek, G. Meijer, A. Osterwalder, and M. R. Tarbutt, Phys. Rev. A **86**, 021404 (2012).

[32] M. Quintero-Pérez, P. Jansen, T. E. Wall, J. E. van den Berg, S. Hoekstra, and H. L. Bethlem, Phys. Rev. Lett. **110**, 133003 (2013).

[33] P. Jansen, M. Quintero-Pérez, T. E. Wall, J. E. van den Berg, S. Hoekstra, and H. L. Bethlem, Phys. Rev. A **88**, 043424 (2013).

[34] J. E. van den Berg, S. C. Mathavan, C. Meinema, J. Nauta, T. H. Nijbroek, K. Jungmann, H. L. Bethlem, and S. Hoekstra, J. Mol. Spectrosc. **300**, 22 (2014), part of the Special Issue: Spectroscopic Tests of Fundamental Physics.

[35] C. Meng, A. P. P. van der Poel, C. Cheng, and H. L. Bethlem, Phys. Rev. A **92**, 023404 (2015).

[36] Y. Shyur, J. A. Bossert, and H. J. Lewandowski, J. Phys. B: At., Mol. Opt. Phys. **51**, 165101 (2018).

[37] Y. Shyur, N. J. Fitch, J. A. Bossert, T. Brown, and H. J. Lewandowski, Rev. Sci. Instrum. **89**, 084705 (2018).

[38] eEDM Collaboration, P. Aggarwal, Y. Yin, K. Esajas, H. L. Bethlem, A. Boeschoten, A. Borschevsky, S. Hoekstra, K. Jungmann, V. R. Marshall, T. B. Meijknecht, M. C. Mooij, R. G. E. Timmermans, A. Touwen, W. Ubachs, and L. Willmann, "Deceleration and trapping of SrF molecules," arXiv:2103.07968 [physics.atom-ph] (2021).

[39] O. A. Krohn, K. J. Catani, J. Greenberg, S. P. Sundar, G. da Silva, and H. J. Lewandowski, J. Chem. Phys. **154**, 074305 (2021).

[40] L. S. Petralia, A. Tsikritea, J. Loreau, T. P. Softley, and B. R. Heazlewood, Nat. Commun. **11**, 173 (2020).

[41] A. Kilaj, H. Gao, D. Rösch, U. Rivero, J. Küpper, and S. Willitsch, Nat. Commun. **9**, 2096 (2018).

[42] T. Yang, A. Li, G. K. Chen, C. Xie, A. G. Suits, W. C. Campbell, H. Guo, and E. R. Hudson, J. Phys. Chem. Lett. **9**, 3555 (2018).

[43] M. T. Bell, A. D. Gingell, J. M. Oldham, T. P. Softley, and S. Willitsch, Faraday Discuss. **142**, 73 (2009).

[44] K. Okada, Y. Takada, N. Kimura, M. Wada, and H. A. Schuessler, Rev. Sci. Instrum. **88**, 083106 (2017).

[45] N. J. Fitch, D. A. Esteves, M. I. Fabrikant, T. C. Briles, Y. Shyur, L. P. Parazzoli, and H. J. Lewandowski, J. Mol. Spectrosc. **278**, 1 (2012).

[46] Y. Shyur, "Stark deceleration methods for cold molecule experiments," Ph.D. thesis, University of Colorado, 2018.

[47] N. J. Fitch, "Traveling-wave Stark-decelerated molecular beams for cold collision experiments," Ph.D. thesis, University of Colorado, 2013.

[48] D. Proch and T. Trickl, Rev. Sci. Instrum. **60**, 713 (1989).

[49] M. I. Fabrikant, T. Li, N. J. Fitch, N. Farrow, J. D. Weinstein, and H. J. Lewandowski, Phys. Rev. A **90**, 033418 (2014).

[50] M. Quintero-Pérez, T. E. Wall, S. Hoekstra, and H. L. Bethlem, J. Mol. Spectrosc. **300**, 112 (2014), part of the Special Issue: Spectroscopic Tests of Fundamental Physics.

[51] L. P. Parazzoli, N. Fitch, D. S. Lobser, and H. J. Lewandowski, New J. Phys. **11**, 055031 (2009).

[52] M. C. McCarthy, S. Mohamed, J. M. Brown, and P. Thaddeus, Proc. Natl. Acad. Sci. U. S. A. **103**, 12263 (2006).

[53] O. Nourbakhsh, J. M. Michan, T. Mittertreiner, D. Carty, E. Wrede, P. Djuricanin, and T. Momose, Mol. Phys. **113**, 4007 (2015).

[54] M. Kirste, X. Wang, H. C. Schewe, G. Meijer, K. Liu, A. van der Avoird, L. M. C. Janssen, K. B. Gubbels, G. C. Groenenboom, and S. Y. T. van de Meerakker, Science **338**, 1060 (2012).

[55] V. A. Cho and R. B. Bernstein, J. Phys. Chem. **95**, 8129 (1991).

[56] P. C. Schmid, J. Greenberg, M. I. Miller, K. Loeffler, and H. J. Lewandowski, Rev. Sci. Instrum. **88**, 123107 (2017).

[57] M. A. Smith and M. Hawley, Int. J. Mass Spectrom. Ion Processes **149–150**, 199 (1995).

[58] J. Hernandes and A. K. T. Assis, Phys. Rev. E **68**, 046611 (2003).

[59] Comsol multiphysics® v. 5.4. COMSOL AB, Stockholm, Sweden.